

Unfolding without Iterations, Adversaries, or Surrogates

Ayodele Ore¹ and Tilman Plehn^{1,2}

¹ Institut für Theoretische Physik, Universität Heidelberg, Germany

² Interdisciplinary Center for Scientific Computing (IWR), Universität Heidelberg, Germany

March 2, 2026

Abstract

Correcting measurements for detector effects and constructing appropriate public data representations is a pressing problem in LHC physics. Current methods solve this inverse problem by relying on iterations, minimax optimization, or a surrogate forward mapping. We introduce Adversary-free Unfolding SanS Iteration or Emulation (AUSSIE), which dispenses with these mechanisms while remaining asymptotically correct. AUSSIE replaces the second OmniFold step with a new loss function that directly yields solutions with minimal dependence on the reference simulation. We showcase AUSSIE on various unfolding tasks, including full-phase-space jet substructure.

Contents

1	Introduction	2
2	Adversary-free Unfolding SanS Iteration or Emulation (AUSSIE)	3
3	Results	7
3.1	Toy example	7
3.2	Jet substructure observables	8
3.3	Jet constituents	11
3.4	Parton-level events	13
4	Outlook	15
A	Training details and hyperparameters	16
B	Numerical details	19
C	Additional jet substructure plots	19
	References	22

1 Introduction

Percent-level measurements at the LHC have changed the way we think about hadron collider physics. A central pillar of this precision program is high-fidelity simulation, connecting Lagrangians with parton-level theory predictions and observables [1]. However, the expense and inaccessibility of these simulations is rapidly becoming a critical bottleneck — it limits the number of hypotheses that can be tested with simulation-based inference and precludes the analysis of data outside each experimental collaboration.

Unfolding provides an alternative strategy by defining appropriate data representations for analyses. It enables efficient comparison to a wide range of models across experiments and shifts the computational cost from repeated detector simulation to a one-time inference [2]. Traditional unfolding methods, however, rely on binning and do not scale to high-dimensional phase spaces [3, 4].

Modern machine learning [5] enables unbinned unfolding in many dimensions [6, 7]. Two broad classes of approaches have emerged. Discriminative methods, like OmniFold [8], train classifiers to reweight a simulated reference to the unfolded distribution [9–12]. This technique has been deployed in several experimental analyses [13–18]. Alternatively, generative neural networks can be trained to sample unfolded events [19–30], with complementary advantages in terms of efficiency and flexibility.

A common part of many unfolding methods is the use of iterative refinement to reduce bias toward the simulated prior and to ensure closure at reconstruction level [8, 31]. While iterations guarantee convergence in principle, the rate of convergence may be slow for substantial forward smearing. This makes iterative strategies computationally expensive since they are fundamentally sequential and cannot be parallelized. Furthermore, because the number of required iterations is not known *a priori*, stopping criteria must be selected heuristically. As a result, residual bias from the simulation can persist if the procedure is terminated prematurely, while excessive iteration may lead to increased variance or overfitting.

A few non-iterative approaches have also been explored. Empirical Bayes approaches with learned forward surrogates [21, 29] avoid explicit simulation dependence, but require expensive sampling and integration over the latent phase space at each training step. Adversarial formulations [10, 19, 32] train a generator on the latent phase space to fool a reconstruction-level discriminator. While efficient, the non-convex minimax optimization inherent to these methods tends to be unstable and sensitive to hyperparameter choices.

We devise a novel approach to unfolding that is non-iterative, accurate, and fast: Adversary-free Unfolding SanS Iteration or Emulation (AUSSIE). AUSSIE is a discriminative unfolding method similar to OmniFold, but with a modified second step that eliminates the need for iterative refinement. By directly finding solutions to the unfolding problem, i.e. latent distributions whose forward mapping matches the data, AUSSIE exhibits drastically reduced dependence on the reference simulation. We demonstrate that AUSSIE consistently finds better solutions than ten OmniFold iterations, as judged by the closure onto pseudodata in the reconstructed and latent phase spaces.

The remainder of this paper is organized as follows. In Section 2, we introduce the preliminaries of unfolding and derive the AUSSIE training objective. Section 3 presents a series of results, starting with a toy Gaussian example before progressing to jet substructure and full parton-level events. In each case, we compare to OmniFold as a benchmark. Finally, Section 4 contains our concluding remarks. We also include three appendices containing additional technical details to facilitate reproducibility.

2 Adversary-free Unfolding SanS Iteration or Emulation (AUSSIE)

Unfolding as an inverse problem deconvolves observations x that arise from distortions of some underlying truth z , for instance, through hadronization or detector interactions. For a stochastic distortion, it involves the following probability densities:

$$\begin{array}{ccc}
 p_{\text{sim}}(z) & \xleftrightarrow{\text{unfolding inference}} & p_{\text{unfold}}(z) \\
 p_{\text{sim}}(x|z) \downarrow & & \uparrow \text{unfold} \\
 p_{\text{sim}}(x) & \xleftrightarrow{\text{forward inference}} & p_{\text{data}}(x)
 \end{array} \quad (1)$$

The latent variable z may be at particle level or parton level, and we use the term part level to cover both cases. The conditional probability $p_{\text{sim}}(x|z)$ is the transfer function characterizing forward simulation applied to z . On the simulation side this implies a forward folding,

$$p_{\text{sim}}(x) = \int dz p_{\text{sim}}(x|z) p_{\text{sim}}(z). \quad (2)$$

In simulation, we have complete access to z and can sample pairs that implicitly encode the forward conditional distribution,

$$(z, x) \sim p_{\text{sim}}(x, z) = p_{\text{sim}}(x|z) p_{\text{sim}}(z). \quad (3)$$

On the data side we just have access to samples from $p_{\text{data}}(x)$. The goal is to find a distribution $p_{\text{unfold}}(z)$ that maps forward to $p_{\text{data}}(x)$ under Eq. (2),

$$p_{\text{data}}(x) = \int dz p_{\text{sim}}(x|z) p_{\text{unfold}}(z). \quad (4)$$

Assuming that the transfer function is an accurate model of the real detector, a solution $p_{\text{unfold}}(z)$ can be interpreted as an estimate for the part-level phase space distribution in data. However, it should be understood that the forward process of the detector acts on the full part-level phase space. As such, the assumption may be violated even for perfect detector simulation if effects that influence the forward process are not included in z [29, 33, 34]. In a similar vein, the definition of $p_{\text{unfold}}(z)$ is influenced by nuisance parameters of the detector simulation [9, 11, 35, 36]. If the simulator is differentiable, then $p_{\text{unfold}}(z)$ can be obtained by maximizing the likelihood of observed data with Eq. (4) by gradient descent.

Density ratio unfolding

We propose Adversary-free Unfolding SanS Iteration or Emulation (AUSSIE). Similar to OmniFold, AUSSIE phrases unfolding in terms of density ratios. At reco level x we define

$$R(x) = \frac{p_{\text{data}}(x)}{p_{\text{sim}}(x)}, \quad (5)$$

and the unfolding target condition in Eq. (4) becomes

$$\begin{aligned}
 R(x) &= \frac{1}{p_{\text{sim}}(x)} \int dz p_{\text{sim}}(x|z) p_{\text{unfold}}(z) \\
 &= \int dz p_{\text{sim}}(z|x) \frac{p_{\text{unfold}}(z)}{p_{\text{sim}}(z)}.
 \end{aligned} \quad (6)$$

If we define the corresponding part-level ratio as

$$\bar{R}(z) \equiv \frac{p_{\text{unfold}}(z)}{p_{\text{sim}}(z)}, \quad (7)$$

the above target relation in terms of density ratios reads

$$R(x) = \int dz p_{\text{sim}}(z|x) \bar{R}(z). \quad (8)$$

In this relation the conditional probability from the forward folding in Eq. (2) is inverted. When unfolding with density ratios, we use the estimate of $\bar{R}(z)$ to construct the unfolded distribution through reweighting

$$p_{\text{unfold}}(z) = \bar{R}(z) p_{\text{sim}}(z). \quad (9)$$

Closure

Because of the non-injective nature of the simulation and a potential loss of information in the forward direction, Eqs. (4) and (8) admit multiple solutions. Consequently, judging $p_{\text{unfold}}(z)$ in terms of agreement with the part-level distribution in a pseudodata sample can be misleading. Moreover, such a test cannot be performed in real data. The part-level problem of ensuring complete coverage of the solution space is an ongoing research question and beyond the scope of our study.

Instead, we first assess the unfolding at reco-level, where a two-sample test between $p_{\text{data}}(x)$ and the forward folding of $p_{\text{unfold}}(z)$ can establish the validity of a solution. In terms of density ratios, we realize this forward folding with the joint probability of part/reco pairs,

$$\int dz p_{\text{sim}}(x, z) \bar{R}(z) \stackrel{\text{Eq. (8)}}{=} R(x) p_{\text{sim}}(x) = p_{\text{data}}(x). \quad (10)$$

Training

As a first step, AUSSIE approximates the reco-level density ratio by training a classifier between samples from $p_{\text{data}}(x)$ and $p_{\text{sim}}(x)$, for example using the binary cross entropy (BCE) loss,

$$R_{\theta}(x) \approx R(x). \quad (11)$$

In the second step, AUSSIE trains a part-level network $\bar{R}_{\varphi}(z)$ such that it forward maps to $R_{\theta}(x)$ as prescribed by Eq. (8). To achieve this, we exploit a maximum likelihood classifier (MLC)-like loss functional,

$$\mathcal{L}_{\text{MLC}}[R_{\theta}, \bar{R}_{\varphi}] = \int dx dz p_{\text{sim}}(x, z) [R_{\theta}(x) - \bar{R}_{\varphi}(z) \log R_{\theta}(x)], \quad (12)$$

which uses paired reco/part events (x, z) from simulation. If we freeze $\bar{R}_{\varphi}(z)$, this is essentially a regression loss for $R_{\theta}(x)$, as we can see from the functional derivative

$$G_{\theta, \varphi}(x) \equiv \frac{\delta \mathcal{L}_{\text{MLC}}[R_{\theta}, \bar{R}_{\varphi}]}{\delta R_{\theta}(x)} = p_{\text{sim}}(x) \left[1 - \frac{1}{R_{\theta}(x)} \int dz p_{\text{sim}}(z|x) \bar{R}_{\varphi}(z) \right]. \quad (13)$$

It vanishes everywhere exactly when the learned version of Eq. (8) holds,

$$R_{\theta}(x) = \int dz p_{\text{sim}}(z|x) \bar{R}_{\varphi}(z). \quad (14)$$

If $R_\theta(x)$ simultaneously satisfies Eqs. (14) and (11), then $\bar{R}_\varphi(z)$ solves the unfolding problem.

Directly optimizing \mathcal{L}_{MLC} with respect to $\bar{R}_\varphi(z)$ does not yield the above unfolding relations, so we need another way to use this result to train the unfolders. The key idea in AUSSIE is to train $\bar{R}_\varphi(z)$ such that the pretrained classifier $R_\theta(x)$ lies at the stationary point of \mathcal{L}_{MLC} . To achieve this, we minimize a norm of $G_{\theta,\varphi}$, now freezing θ and varying φ . For a function-space object, the natural choice of norm is the Reproducing Kernel Hilbert Space (RKHS) norm

$$\|G_{\theta,\varphi}\|_{\mathcal{H}}^2 \equiv \int dx dx' G_{\theta,\varphi}(x) K(x, x') G_{\theta,\varphi}(x'), \quad (15)$$

with K a positive semi-definite kernel. K should not be confused with a detector response kernel, as it couples pairs of reco-level events.

The RKHS norm is minimized at zero when $G_{\theta,\varphi}(x)$ lies in the null space of K . For a strictly positive-definite kernel this occurs only when $G_{\theta,\varphi}(x)$ is pointwise zero, implying that the unfolding condition is satisfied. Repeating the above analysis with an appropriate BCE or Mean Squared Error (MSE) loss recovers the same result.

AUSSIE performs unfolding by minimizing the RKHS norm, inverting the integral relation from Eq. (8). We consider the following two options for implementing Eq. (15) as a loss function:

Analytic kernel We can use a closed-form and positive-definite kernel, for example a Gaussian

$$K(x, x') = \exp \frac{-|x - x'|^2}{2\Lambda^2}, \quad (16)$$

where Λ is a scale hyperparameter. The RKHS-norm in Eq. (15) can then be directly evaluated by rearranging Eq. (13) as a double expectation over paired part/reco samples

$$\mathcal{L}_{\text{Gauss}}[\bar{R}_\varphi] = \left\langle \left(1 - \frac{\bar{R}_\varphi(z)}{R_\theta(x)} \right) K(x, x') \left(1 - \frac{\bar{R}_\varphi(z')}{R_\theta(x')} \right) \right\rangle_{p_{\text{sim}}(x,z) p_{\text{sim}}(x',z')} \quad (17)$$

which follows by pulling out the integral and probability densities from $G_{\theta,\varphi}(x)$.

AutoDiff Interestingly, taking the parameter gradient norm

$$|\nabla_\theta \mathcal{L}_{\text{MLC}}|^2 = \sum_{\theta_i} (\nabla_{\theta_i} \mathcal{L}_{\text{MLC}}[R_\theta, \bar{R}_\varphi])^2, \quad (18)$$

is equivalent to Eq. (15) with K chosen as the Neural Tangent Kernel (NTK) [37, 38],

$$\begin{aligned} |\nabla_\theta \mathcal{L}_{\text{MLC}}|^2 &= \sum_{\theta_i} \left(\int dx \frac{\delta \mathcal{L}_{\text{MLC}}[R_\theta, \bar{R}_\varphi]}{\delta R_\theta(x)} \nabla_{\theta_i} R_\theta(x) \right)^2 \\ &= \sum_{\theta_i} \left(\int dx G_{\theta,\varphi}(x) \nabla_{\theta_i} R_\theta(x) \right)^2 \\ &= \int dx dx' G_{\theta,\varphi}(x) G_{\theta,\varphi}(x') \sum_{\theta_i} \nabla_{\theta_i} R_\theta(x) \nabla_{\theta_i} R_\theta(x'). \\ &= \|G_{\theta,\varphi}\|_{\mathcal{H}}^2 \quad \text{with} \quad K(x, x') = \sum_{\theta_i} \nabla_{\theta_i} R_\theta(x) \nabla_{\theta_i} R_\theta(x'). \end{aligned} \quad (19)$$

The NTK is strictly positive definite in the infinite-width limit but positive semi-definite for finite θ . Therefore minimizing Eq. (18) only guarantees that $G_{\theta,\varphi}$ is pointwise zero

if it is in the tangent space of $R_\theta(x)$, i.e. if the classifier is sufficiently expressive. We expect this to be satisfied since $G_{\theta,\varphi}$ is a simple function of $R_\theta(x)$ and we match the architecture with $R_\varphi(x)$.

Numerically, we find that using the L_1 gradient norm

$$\mathcal{L}_{\text{AutoDiff}}[\bar{R}_\varphi] = \sum_{\theta_i} |\nabla_{\theta_i} \mathcal{L}_{\text{MLC}}[R_\theta, \bar{R}_\varphi]| \quad (20)$$

gives better results, so we will use this loss function for our following studies. It shares the same optimal asymptotic limit as Eq. (18) despite not having a kernel interpretation. To evaluate $\mathcal{L}_{\text{AutoDiff}}$, we apply the autograd engine in PyTorch to the Monte Carlo estimate of \mathcal{L}_{MLC} . Further numerical details are provided in Appendix B.

These two options are complementary. The fixed analytic kernel is computationally efficient, but introduces a hyperparameter and does not translate easily to non-trivial representations of x , such as point clouds. The AutoDiff loss is more expensive to compute, but has no hyperparameters and exploits all symmetries encoded in the architecture of $R_\theta(x)$. Given these considerations, we prefer $\mathcal{L}_{\text{Gauss}}$ for low-dimensional x and $\mathcal{L}_{\text{AutoDiff}}$ for high-dimensional x .

OmniFold comparison

It is instructive to briefly compare AUSSIE to OmniFold. OmniFold also trains a classifier $\omega(x) \equiv R_\theta(x)$ to learn the reco-level density ratio as in Eq. (11). In a second step, it trains $\nu(z) \equiv \bar{R}_\varphi(z)$ to regress $\omega(x)$, originally using a BCE loss. For consistency, we write the equivalent MLC loss

$$\mathcal{L}_{\text{OmniFold}}[\omega, \nu] = \int dx dz p_{\text{sim}}(x, z) [\nu(z) - \omega(x) \log \nu(z)]. \quad (21)$$

This leads to the following solution for OmniFold

$$\nu(z) = \int dx p_{\text{sim}}(x|z) \omega(x). \quad (22)$$

This condition is an ‘inversion’ of the unfolding target relation in Eq. (8). As a result, the forward folding of this part-level ratio does not in general produce the correct reco-level ratio,

$$\begin{aligned} \omega(x) &\stackrel{?}{=} \int dz p_{\text{sim}}(z|x) \nu(z) \\ &= \int dz p_{\text{sim}}(z|x) \int dx' p_{\text{sim}}(x'|z) \omega(x') \\ &= \int dx' dz p_{\text{sim}}(x'|z) p_{\text{sim}}(z|x) \omega(x') \\ \Leftrightarrow &\int dz p(x'|z) p(z|x) = \delta(x' - x). \end{aligned} \quad (23)$$

The unfolding only closes for a completely invertible detector. For stochastic detectors, the OmniFold weight from Eq. (22) is in a sense double-smeared, and cannot completely map $p_{\text{sim}}(z)$ onto $p_{\text{unfold}}(z)$. To account for this, OmniFold iterates the reweighting and regression to converge on a solution. By viewing these iterations as expectation-maximization steps, the authors of OmniFold showed that it is guaranteed to converge to a solution of Eq. (8).

3 Results

We benchmark the performance of AUSSIE on a set of increasingly complex unfolding problems. We start with a Gaussian toy example in Section 3.1 before unfolding detector effects on jets via substructure observables in Section 3.2 and via the full constituent-level phase space in Section 3.3. Finally, we show parton-level unfolding for a tHj process in Section 3.4.

3.1 Toy example

We begin with a simple Gaussian example where the forward map imparts a large smearing,

$$\begin{aligned} p_{\text{sim}}(z) &= \mathcal{N}(z; 0, 1) & \text{and} & & p(x|z) &= \mathcal{N}(x; z, 2). \end{aligned} \quad (24)$$

For this one-dimensional problem, we train AUSSIE using small MLP networks for R_θ and \bar{R}_φ and the Gaussian kernel loss from Eq. (17). We make no attempt to optimize the hyperparameter Λ and simply set it to one. For comparison, we also train OmniFold using the same network configurations for up to 20 iterations.

In Figure 1 we show the results of the unfolding for reco level (left) and part level (right). AUSSIE achieves perfect closure on reco level and near perfect closure on part level. The solutions on part level are somewhat degenerate due to the finite statistics of the training sample. Comparing this result to a single iteration of OmniFold, the misspecified objective in Eq. (22) manifests as a poor reweighting on the part and reco levels. OmniFold improves with iterations, but the large smearing means that 20 iterations are not quite sufficient for convergence.

To highlight the different training dynamics of AUSSIE and OmniFold, we trace their convergence with respect to the analytic solution of our toy problem. Using Eq. (24), we determine the true functions $R(x)$ and $\bar{R}(z)$ and calculate the corresponding values of \mathcal{L}_{MLC} and $\mathcal{L}_{\text{OmniFold}}$ over the test dataset. Figure 2 tracks the loss values for the two second-step networks of AUSSIE and OmniFold. The single AUSSIE classifier and 20 OmniFold classifiers are omitted. In the top panel we see that both methods approach the solution $\bar{R}(z)$, although the

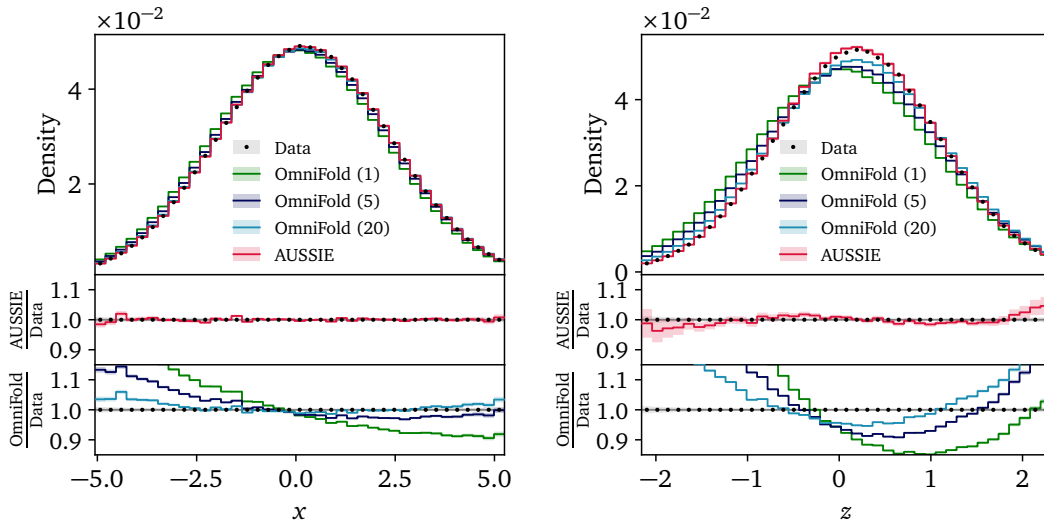


Figure 1: **Gaussian toy example:** Observable feature x (left) and unfolded feature z (right), comparing AUSSIE and various iterations of OmniFold.

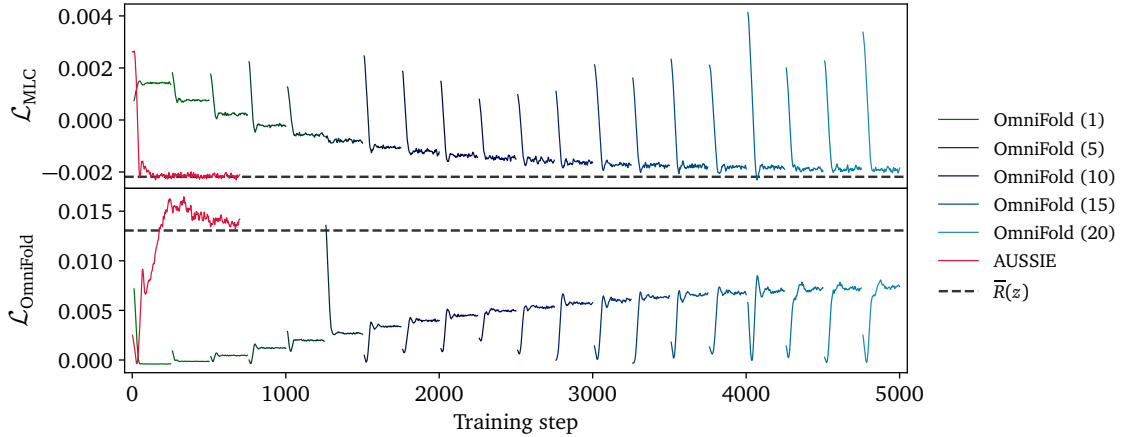


Figure 2: **Regression losses tracked over training:** (Top) The \mathcal{L}_{MLC} loss, whose optimum enforces the unfolding condition. (Bottom) The $\mathcal{L}_{\text{OmniFold}}$ loss, which is an inversion of \mathcal{L}_{MLC} . The black dashed line shows the value of each loss for the optimal solution $\bar{R}(z)$. Note that $\mathcal{L}_{\text{OmniFold}}$ is only the direct objective for the first OmniFold iteration.

convergence is significantly faster for AUSSIE. The bottom panel reveals the cause; $\bar{R}(z)$ is not a minimizer of $\mathcal{L}_{\text{OmniFold}}$ and thus each regression step of OmniFold spends unnecessary computation. We refrain from explicit timing measurements in this study because a fair assessment would require extensive optimization of the hyperparameters related to iteration.

3.2 Jet substructure observables

As our first physics example, we unfold detector effects on jet substructure observables in Zj events. The standard dataset [8] consists of $R=0.4$ anti- k_T jets with $p_T > 150$ GeV that are generated with different parton showers but passed through the same DELPHES v3.4.2 [39] simulation of the CMS detector. The reco-level jets are defined with the same clustering algorithm. For the reference simulation p_{sim} , we take the ATLAS A14 PYTHIA v8.243 central tune sample, which contains 1.6M jets. An equal-sized sample showered with HERWIG v7.1.5 is also provided. The aim is to unfold the following six jet substructure observables

$$x, z = \left\{ \begin{array}{lll} \text{Jet mass } m & \text{N-subjettiness ratio } \tau_{21} & \text{Groomed momentum fraction } z_g \\ \text{Jet width } w & \text{Jet multiplicity } N & \text{Groomed mass } \log \rho \end{array} \right\}. \quad (25)$$

Unfolding high-level observables induces a dependence on the reference distribution in the results [33, 34]. This is because the assumption that the forward mapping in simulations matches the one in data is violated — transfer functions between high-level observables involve an integral over the part-level phase space of the given distribution. In a real measurement, this ‘hidden-variables’ effect should be treated as a systematic uncertainty [33], or avoided by unfolding the full particle-level phase space [30]. We sidestep this issue for now and define the pseudodata as a reweighting of the PYTHIA reference, where the weights are obtained from a classifier trained between PYTHIA and HERWIG on the part-level substructure observables,

$$p_{\text{data}}(x, z) \equiv D(z) p_{\text{PYTHIA}}(x, z) \quad \text{with} \quad D(z) \approx \frac{p_{\text{HERWIG}}(z)}{p_{\text{PYTHIA}}(z)}. \quad (26)$$

We train AUSSIE in this setting, again using simple MLPs and the Gaussian Kernel loss in Eq. (17) with $\Lambda = 1$. We also perform ten iterations of OmniFold for reference.

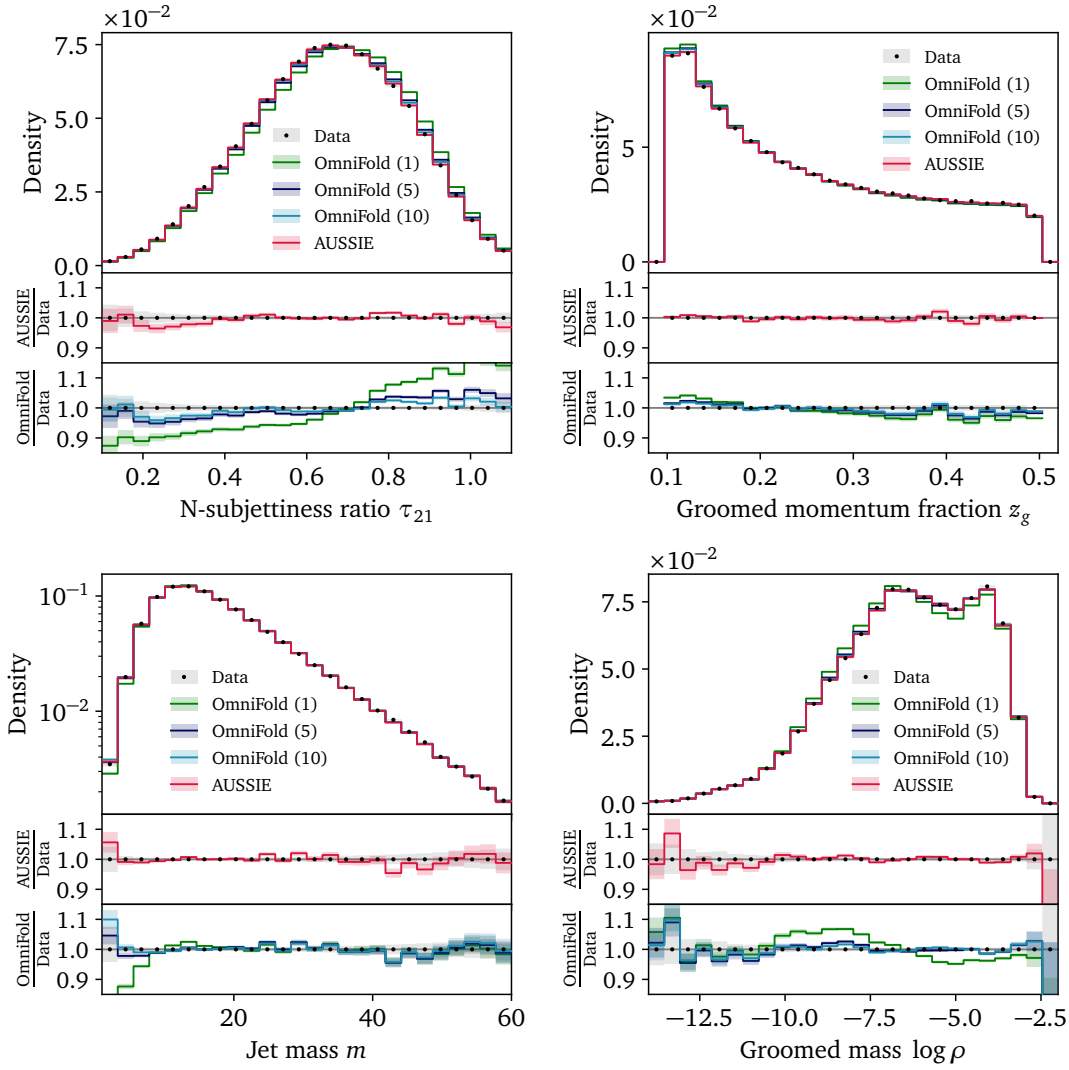


Figure 3: **Reco-level jet substructure**, comparing AUSSIE and various iterations of OmniFold.

We show the reco-level results for the substructure observables in Figure 3. AUSSIE matches the data at the order of one percent in each observable, whereas OmniFold exhibits a non-closure in its first iteration. After ten iterations, OmniFold converges to closure but does not match the precision of AUSSIE for τ_{21} or z_g .

In Figure 4 we summarize the reco-level performance using the score of the first-step classifier $R_\theta(x)$, which approximates the optimal observable. AUSSIE maps the lower tail precisely while the upper tail shows a small deviation. OmniFold also reaches relatively high precision after ten iterations, but remains slightly biased toward the simulation as evidenced by the excess in the lower tail.

Finally, in Figure 5 we see that the non-convergence of OmniFold is most evident on part level. It now also shows significant deviations from truth in the jet mass, in addition to τ_{21} and z_g . AUSSIE is more consistent with truth, with deviations being limited to the tails. Since we already observed a tight closure for AUSSIE on reco-level, these deviations mostly reflect the degenerate solution space.

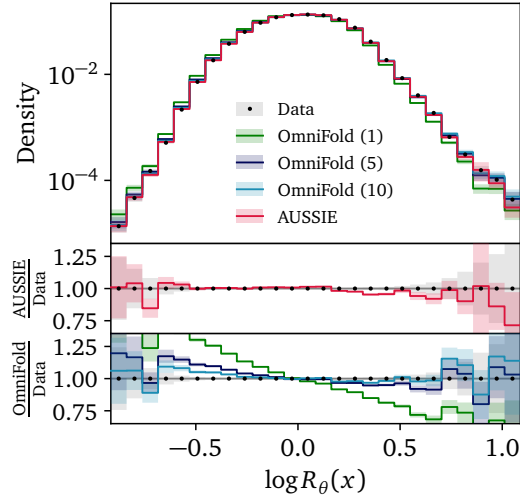


Figure 4: **Reco-level classifier score over jet substructure observables**, comparing AUSSIE and various iterations of OmniFold.

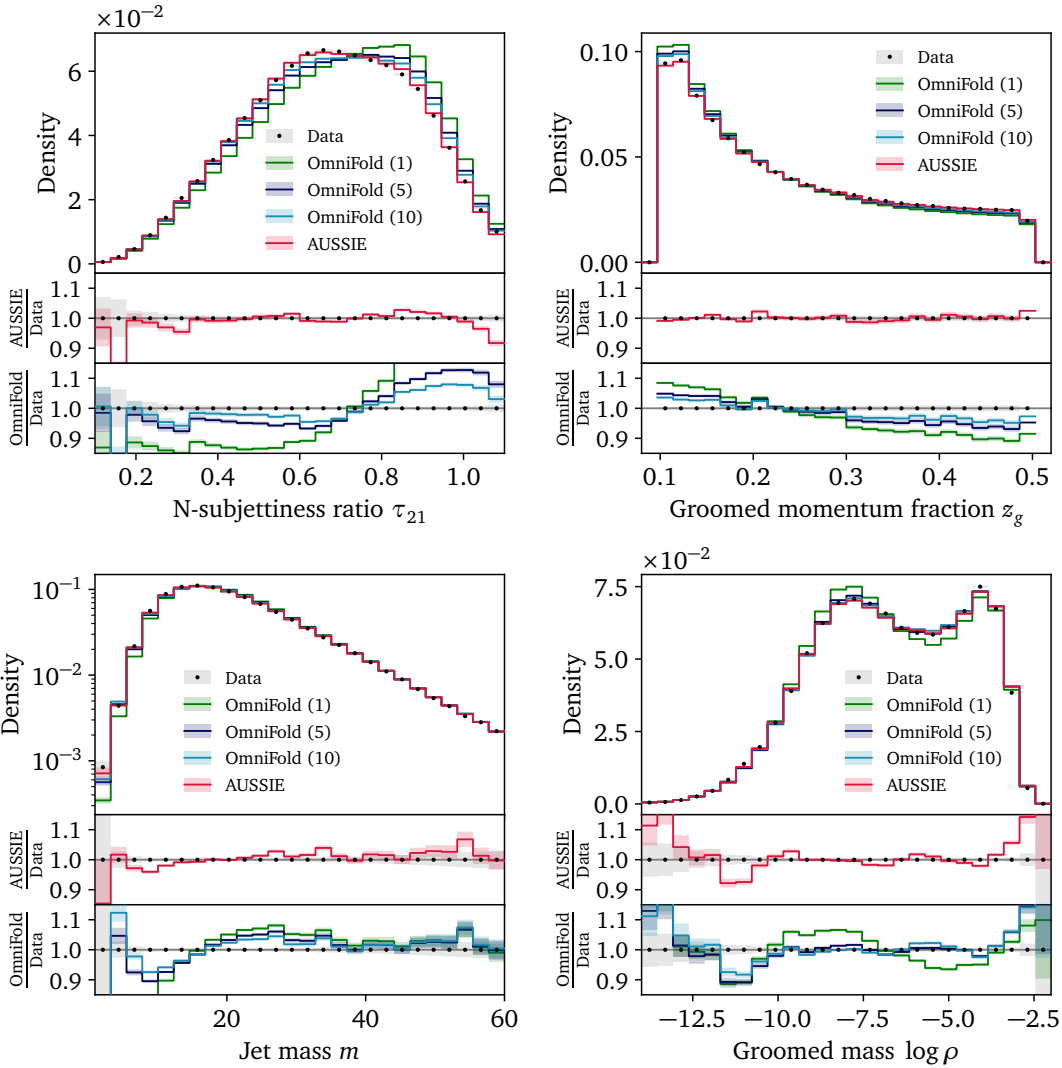


Figure 5: **Unfolded part-level jet substructure**, comparing AUSSIE and various iterations of OmniFold

3.3 Jet constituents

A straightforward solution to the hidden-variables problem, and the proper unfolding task for public data, is to unfold all jet constituents. Since the forward detector simulation naturally acts on this phase space, the unfolding assumption of a universal transfer function is valid, at least up to nuisance parameters. We study AUSSIE in this setting and, accordingly, take the HERWIG sample from the jet dataset as the pseudodata, in contrast to Eq. (26). The vastly increased dimensionality of this unfolding problem poses a significant challenge.

We represent the part-level and reco-level jets as sets of constituent four momenta and now use LGATr networks [40, 41] for $R_\theta(x)$ and $\bar{R}_\varphi(z)$ to exploit the Lorentz and permutation symmetries. For the same reason, and to handle events with varying length, we also switch from the Gaussian kernel loss to the AutoDiff loss from Eq. (20).

Starting with reco-level, we show the jet substructure observables in Figure 6, this time calculated using the recorded constituents. The difference between AUSSIE and OmniFold at reco-level is smaller than in the high-level case from Figure 3. This is because the forward map now corresponds to the true action of the detector simulation, which is only a modest

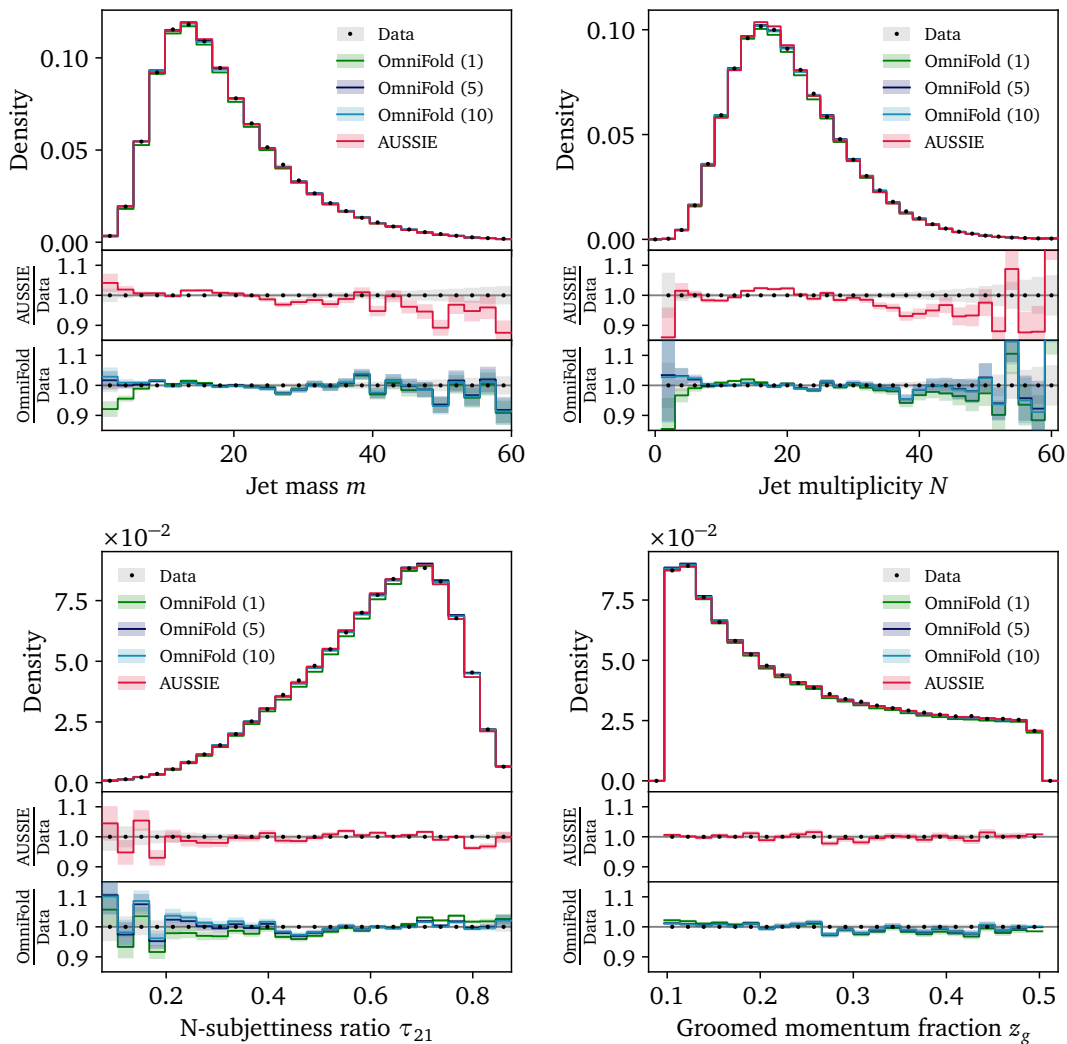


Figure 6: **Reco-level jet substructure (using constituents)**, comparing AUSSIE and various iterations of OmniFold.

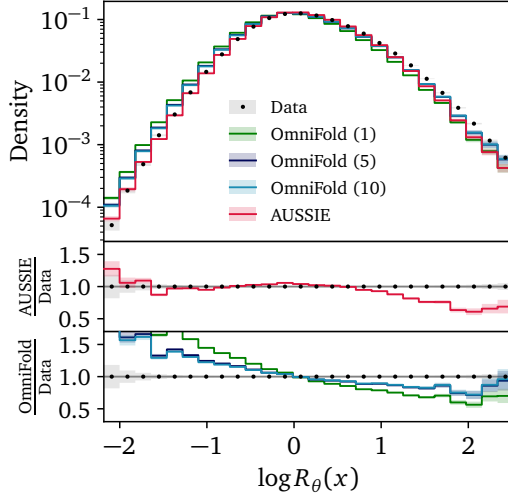


Figure 7: **Reco-level classifier score over constituent-level jets**, comparing AUSSIE and various iterations of OmniFold.

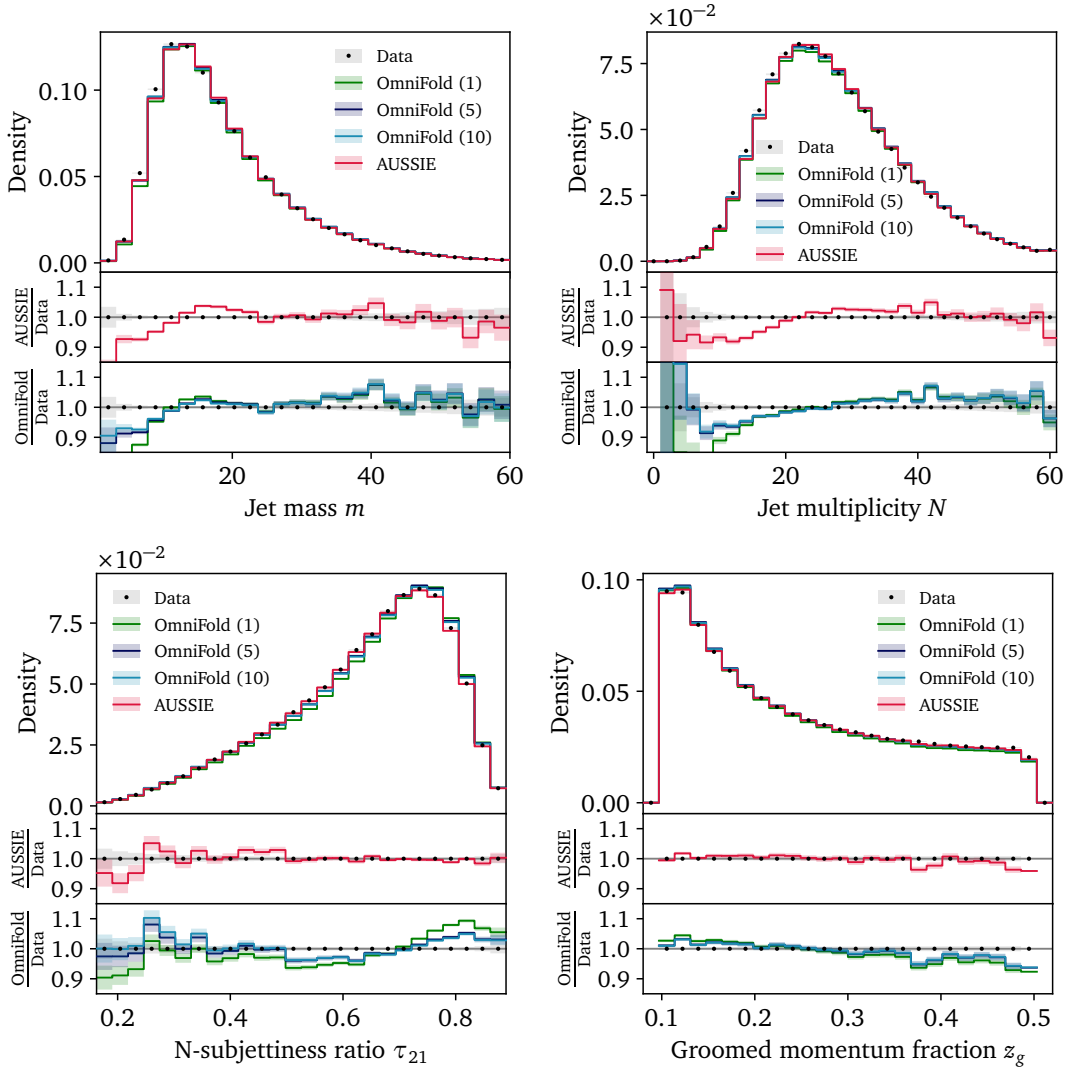


Figure 8: **Unfolded part-level jet substructure (using constituents)**, comparing AUSSIE and various iterations of OmniFold.

smearing. As a result OmniFold now shows better closure in its first iteration. AUSSIE still improves on iteration ten of OmniFold in τ_{21} and z_g , but varies slightly more in the jet mass and multiplicity. However, the classifier score in Figure 7 shows that these marginals obscure information in other constituent-level correlations. While neither AUSSIE nor OmniFold completely reweights the classifier score to match data, AUSSIE does correct the lower tail indicating a better closure in the full phase space. Unlike the previous result using the high-level jet substructure observables, there is no significant improvement for OmniFold between iterations 5 and 10.

On part-level, in Figure 8, we find that neither approach closes exactly onto the HERWIG truth. The jet mass and multiplicity show deviations on the order of ten percent for both methods. Still, τ_{21} and z_g are recovered well by AUSSIE while the OmniFold iterations stagnate with larger bias. As discussed earlier, one cannot expect the part-level distributions to match while observing non-closure at reco level. In this case, we find that the high dimensionality is even a challenge for the step-one classifier. Both AUSSIE and OmniFold are likely to benefit from a larger dataset or transfer learning from pretrained networks [42–44].

3.4 Parton-level events

As a final example, we showcase AUSSIE for unfolding to parton level, which is relevant for parameter inference with the ML-Matrix Element Method [45, 46]. Reweighting-based unfolding is well suited to this scenario since it automatically preserves strict correlations such as momentum conservation and on-shell conditions. However, as we will shortly demonstrate, the high degree of information loss in this setting poses a challenge to iterative methods such as OmniFold.

We consider associated single-top and Higgs production [45, 46]

$$pp \rightarrow tHj \rightarrow (bjj)(\gamma\gamma)j + \text{ISR}, \quad (27)$$

where the top quark decays hadronically and the Higgs decays to photons. ISR introduces additional jets at reco level, effectively causing a combinatorial smearing that prevents clean reconstruction of the top. This process provides sensitivity to the CP phase in the top-Yukawa coupling and is a prime use case for machine learning due to its small cross section in the Standard Model.

We use the dataset from Ref. [47], which considers a varying CP angle $\alpha \in (-\pi, \pi]$, defined through the Yukawa

$$\mathcal{L}_{t\bar{t}H} = -\frac{y_t}{\sqrt{2}} \left[\cos \alpha t\bar{t} + \frac{2i}{3} \sin \alpha t\gamma_5 \bar{t} \right] H. \quad (28)$$

The reference simulation samples α uniformly while the pseudodata fixes the angle,

$$p_{\text{sim}}(z) = \left\langle \frac{1}{\sigma(\alpha)} \frac{d\sigma(\alpha)}{dz} \right\rangle_{\alpha \sim \mathcal{U}[-\pi, \pi]}, \quad p_{\text{data}}(z) = \frac{1}{\sigma(\alpha)} \frac{d\sigma(\alpha)}{dz} \Big|_{\alpha=\pi/4}. \quad (29)$$

The parton-level events are generated by MADGRAPH5 v3.1.0 with LO-NNPDF, showered with PYTHIA, and passed to DELPHES for detector simulation and reconstruction of $R = 0.4$ anti- k_T jets. We keep at most four ISR jets in the reco events, for a maximum of ten total objects. The dataset contains 6.8M reference simulation events and 440k pseudodata events. For more specifics on the process we refer the reader to Ref. [47].

Just as in the constituent unfolding above, here we apply LGATr networks and the AutoDiff loss to the full part-level and reco-level phase spaces. The reco-level results with AUSSIE and

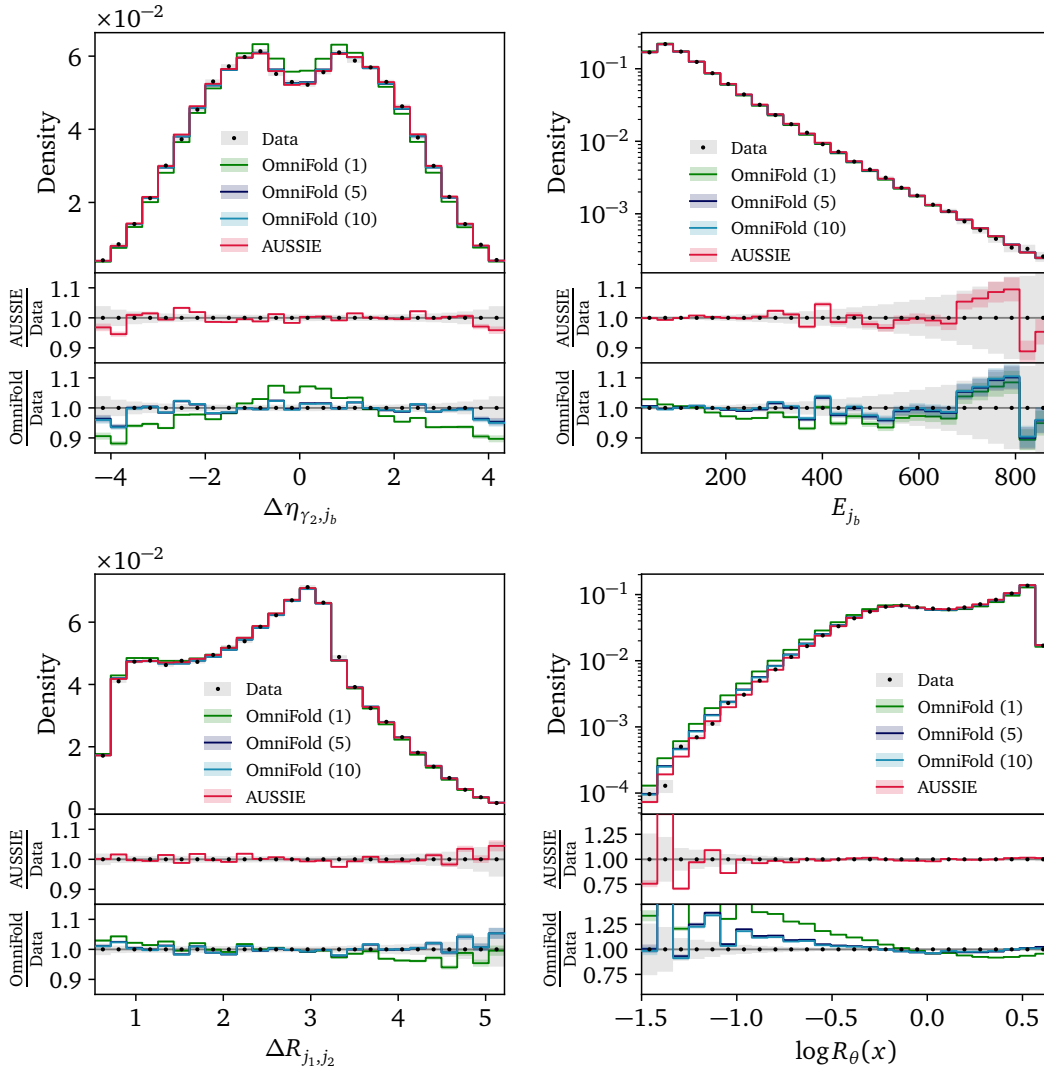


Figure 9: **Reco-level observables in tHj events**, comparing AUSSIE and various iterations of OmniFold. The lower-right panel is the first-step classifier score.

OmniFold are shown in Figure 9. In addition to three kinematic variables that are sensitive to the CP angle, we also include the first-step classifier approximation of the optimal reco-level observable. AUSSIE produces perfect closure in all of these variables, including the classifier score. Even after iterating, OmniFold retains deviations in the tails of the kinematic variables that become apparent in the classifier score. As in the previous section, OmniFold does not noticeably improve from iteration five and ten. We have also checked that no intermediate iteration matches AUSSIE.

We show a selection of part-level distributions in Figure 10. As we have seen before, the advantage of AUSSIE is magnified for part level, compared to reco level. Specifically, angular correlations are reproduced to within statistical fluctuations by AUSSIE, even in regions where OmniFold fails to converge. While OmniFold and AUSSIE both perform well for this benchmark process, we find no observables in which AUSSIE does not improve at least slightly.

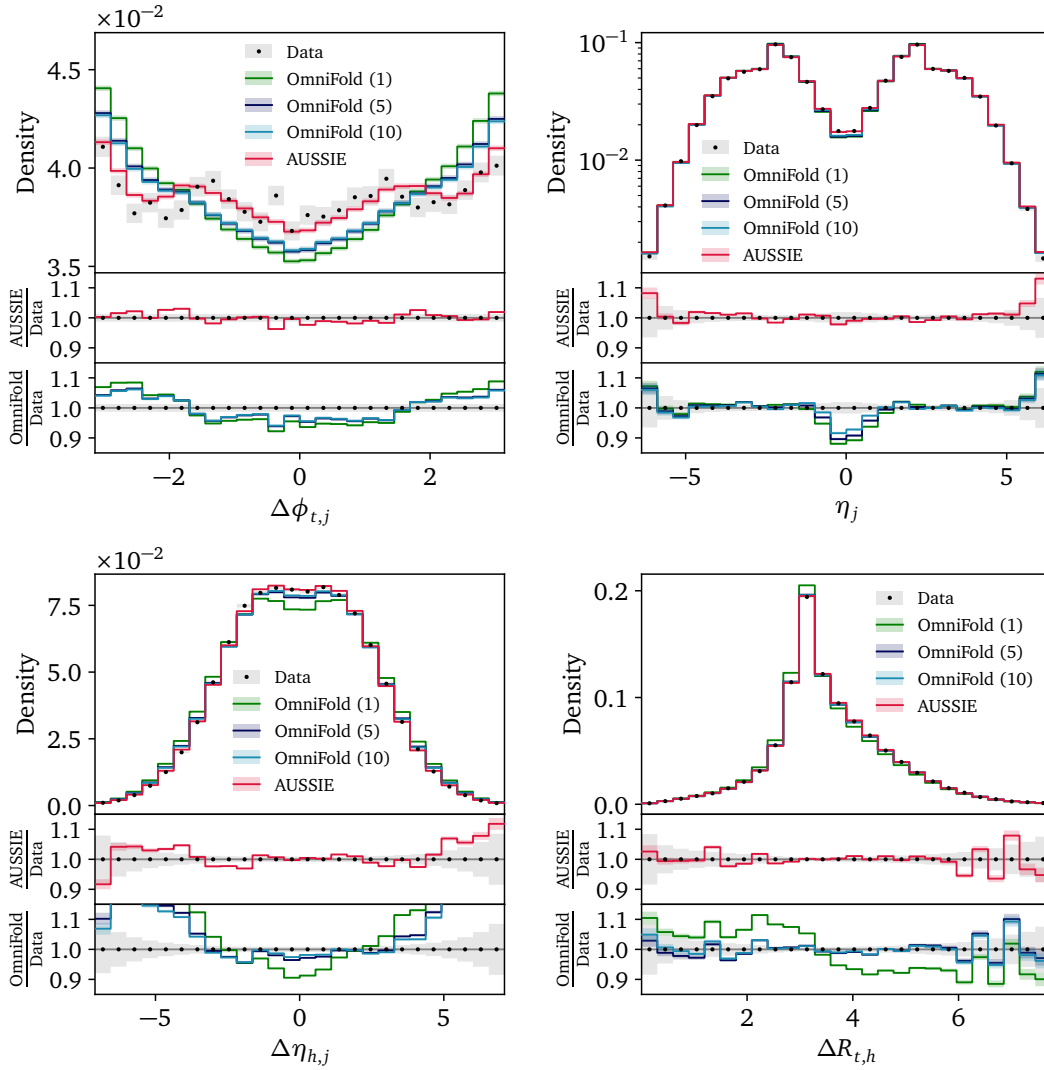


Figure 10: **Unfolded parton-level features in tHj events**, comparing AUSSIE and various iterations of OmniFold.

4 Outlook

We introduced Adversary-free Unfolding SanS Iteration or Emulation (AUSSIE), a novel method for unbinned unfolding of multidimensional collider observables. AUSSIE is a two-step algorithm based on reweighting a simulated dataset that numerically inverts the integral equation relating latent and observable phase spaces. Importantly, it is non-iterative and does not suffer from explicit dependence on the simulated dataset. To our knowledge, AUSSIE is the only unfolding method that achieves this without relying on surrogates or adversarial training.

We demonstrated the performance of AUSSIE on three physics scenarios: unfolding detector effects on jets at the level of substructure observables and at the level of constituents, as well as complete event unfolding to parton level. AUSSIE consistently yields more accurate unfolded distributions than ten iterations of OmniFold, showing better closure in both the reco-level and part-level phase spaces. For experimental effects such as irreducible backgrounds and imperfect acceptance or efficiency, AUSSIE can be readily combined with existing techniques [12, 34].

While we have showcased AUSSIE for the task of unfolding, it is more generally a tool for

efficient simulation-based inference which we expect to apply more broadly.

Acknowledgments

We acknowledge support by the Deutsche Forschungsgemeinschaft (DFG, German Research Foundation) under grant 396021762 – TRR 257: *Particle Physics Phenomenology after the Higgs Discovery*, and through Germany’s Excellence Strategy EXC 2181/1 – 390900948 (the *Heidelberg STRUCTURES Excellence Cluster*). We acknowledge support by the state of Baden-Württemberg through bwHPC and the German Research Foundation (DFG) through grant INST 35/1597-1 FUGG. This project started at the Kavli Institute for Theoretical Physics (KITP) supported by grant NSF PHY-2309135.

Code availability

The code for AUSSIE can be found at <https://github.com/heidelberg-hepml/aussie>.

A Training details and hyperparameters

Toy example

For the Gaussian toy example from Section 3.1, we do not use any preprocessing. The full set of network and optimization hyperparameters are listed in Table 1.

Jet substructure

As preprocessing for the substructure observables in the jet dataset from Section 3.2, we first apply a logarithmic scaling at both part and reco level:

$$m \rightarrow \log m, \quad \tau_{21} \rightarrow \log \tau_{21}, \quad N \rightarrow \log N, \quad w \rightarrow \log w. \quad (30)$$

All features are then standardized to zero mean and unit variance, using separate transformations for x and z calculated with the training split of the reference simulation. The full set of network and optimization hyperparameters are listed in Table 2. The network used to train $D(z)$ as defined in Eq. (26) shares the same MLP architecture as the classifier and unfold.

Constituent-level jets

For the jet constituent example in Section 3.3, we apply preprocessing compatible with the equivariance constraints of the LGATr architecture. All four momenta are represented in cartesian coordinates (E, p_x, p_y, p_z) and preprocessed by boosting into the center-of-mass frame of the jet. Particle identities are one-hot encoded and enter the network as scalar channels. To allow for symmetry breaking, reference vectors indicating the time and beam-transverse directions,

$$\{(1, 0, 0, 0), (1, 0, 0, 1), (1, 0, 0, -1)\}, \quad (31)$$

are appended to the collection of particles before preprocessing with a unique scalar identifier. The full set of network and optimization hyperparameters are listed in Table 3.

	Classifier R_θ	Unfolder \bar{R}_φ
MLP hidden channels	2	2
MLP hidden layers	32	32
MLP activation	SiLU	SiLU
N_{data}	10M	-
N_{sim}	10M	10M
Train/Val/Test	60/5/35	60/5/35
Optimizer	ScheduleFree AdamW	ScheduleFree AdamW
Learning rate	5×10^{-3}	5×10^{-3}
Batch size	8192	8192
Epochs	1	1
Weight decay	0	0
Warmup steps	200	200

Table 1: Network and optimization hyperparameters for AUSSIE and OmniFold on the Gaussian toy example from Section 3.1.

	Classifier R_θ	Unfolder \bar{R}_φ
Architecture	MLP	MLP
Hidden channels	128	128
Hidden layers	4	4
Activation	SiLU	SiLU
N_{data}	1.6M	-
N_{sim}	1.6M	1.6M
Train/Val/Test	60/5/35	60/5/35
Optimizer	ScheduleFree AdamW	ScheduleFree AdamW
Learning rate	5×10^{-4}	10^{-3}
Batch size	1024	8192
Epochs	200	500
Patience	50	50
Weight decay	0	0
Warmup steps	5000	5000

Table 2: Network and optimization hyperparameters for AUSSIE and OmniFold on the substructure-level jet dataset from Section 3.2.

Parton-level events

For the tHj example in Section 3.4, we also use Lorentz-equivariant preprocessing. However, instead of boosting events we globally scale the four-momenta by 1/450 GeV and 1/140 GeV at the part and reco levels respectively. All reco light jets share the same scalar particle identifier, and we add the same symmetry-breaking reference vectors from Eq. (31). The full set of network and optimization hyperparameters are listed in Table 4.

	Classifier R_θ	Unfolder \bar{R}_φ
Architecture	LGATr Slim	LGATr Slim
Blocks	4	4
Heads	4	4
Scalar channels	64	64
Vector channels	32	16
MLP ratio	4	4
Activation	GELU	GELU
Dropout	0.01	0.01
N_{data}	1.6M	-
N_{sim}	1.6M	1.6M
Train/Val/Test	60/5/35	60/5/35
Optimizer	ScheduleFree AdamW	ScheduleFree AdamW
Learning rate	10^{-3}	5×10^{-3}
Batch size	256	2048
Epochs	500	500
Patience	50	50
Weight decay	0	0
Warmup steps	5000	5000

Table 3: Network and optimization hyperparameters for AUSSIE and OmniFold on the constituent-level jet dataset from Section 3.2.

	Classifier R_θ	Unfolder \bar{R}_φ
Architecture	LGATr Slim	LGATr Slim
Blocks	4	4
Heads	4	4
Scalar channels	32	32
Vector channels	8	8
MLP ratio	2	2
Activation	GELU	GELU
N_{data}	440k	-
N_{sim}	6.8M	6.8M
Train/Val/Test	60/5/35	60/5/35
Optimizer	ScheduleFree AdamW	ScheduleFree AdamW
Learning rate	10^{-3}	5×10^{-3}
Batch size	512	8192
Epochs	500	500
Patience	50	50
Weight decay	0	0
Warmup steps	5000	5000

Table 4: Network and optimization hyperparameters for AUSSIE and OmniFold on the tHj dataset from Section 3.4.

B Numerical details

Here we give details on the numerical estimation of the two losses described in the main text.

Kernel loss: The loss from Eq. (17) can be estimated by coupling paired batch elements via a kernel matrix,

$$\mathcal{L}_{\text{Gauss}} \approx \frac{1}{M(M-1)} \sum_{i,j=1}^M \left[\left(1 - \frac{\bar{R}_\varphi(z_i)}{R_\theta(x_i)} \right) K(x_i, x_j) (1 - \delta_{ij}) \left(1 - \frac{\bar{R}_\varphi(z_j)}{R_\theta(x_j)} \right) \right]. \quad (32)$$

By zeroing the diagonal of the matrix, this ‘U-statistic’ estimator is unbiased. The resulting squared norm can occasionally take small negative values due to numerical precision, so we clamp it to stabilize optimization.

AutoDiff loss: The squared L_2 norm from Eq. (18) can be directly computed over a batch by evaluating

$$|\nabla_\theta \mathcal{L}_{\text{MLC}}|^2 \approx \left| \frac{1}{M} \nabla_\theta \sum_{i=1}^M \ell(x_i, z_i) \right|^2 \quad \text{with} \quad \ell(x, z) \equiv R_\theta(x) - \bar{R}_\varphi(z) \log R_\theta(x). \quad (33)$$

While this estimator is straightforward to implement with automatic differentiation, it is biased at finite batch size: the square induces a strictly positive contribution from gradient noise proportional to its variance. This additive variance term vanishes in the limit of large batches. This also explains why we find better performance with the L_1 alternative from Eq. (20), since its linear scaling suppresses this bias compared to the quadratic of the L_2 .

An unbiased estimator for the squared L_2 norm can be constructed by partitioning the batch into two (or more) disjoint subsets and forming the inner product of their parameter gradients.

$$|\nabla_\theta \mathcal{L}_{\text{MLC}}|^2 \approx \left[\frac{1}{P} \nabla_\theta \sum_{i=1}^P \ell(x_i, z_i) \right]^T \left[\frac{1}{M-P} \nabla_\theta \sum_{j=P+1}^M \ell(x_j, z_j) \right]. \quad (34)$$

This two-sample estimator is consistent and removes the additive bias from gradient variance. However, it can fluctuate below zero, making stable optimization difficult. As in the kernel case, larger batch sizes significantly reduce this effect. The optimization can be stabilized by clamping the norm at the cost of some bias. For our studies, we found the L_1 norm from Eq. (20) more favorable, though this may differ depending on the application.

C Additional jet substructure plots

For completeness, we provide the reco-level and part-level distributions for the substructure observables that were omitted from the main text. Figures 11 and 12 respectively show the reco-level and part-level results for the jet multiplicity and width using the high-level dataset. Figures 13 and 14 the results for the jet multiplicity and groomed mass.

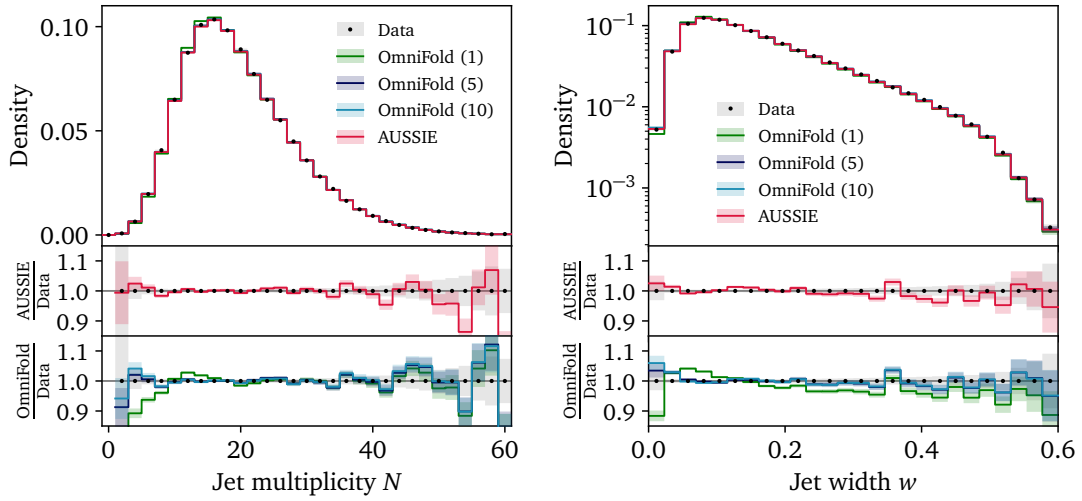


Figure 11: Reco-level jet substructure, comparing AUSSIE and various iterations of OmniFold. Supplements Figure 3.

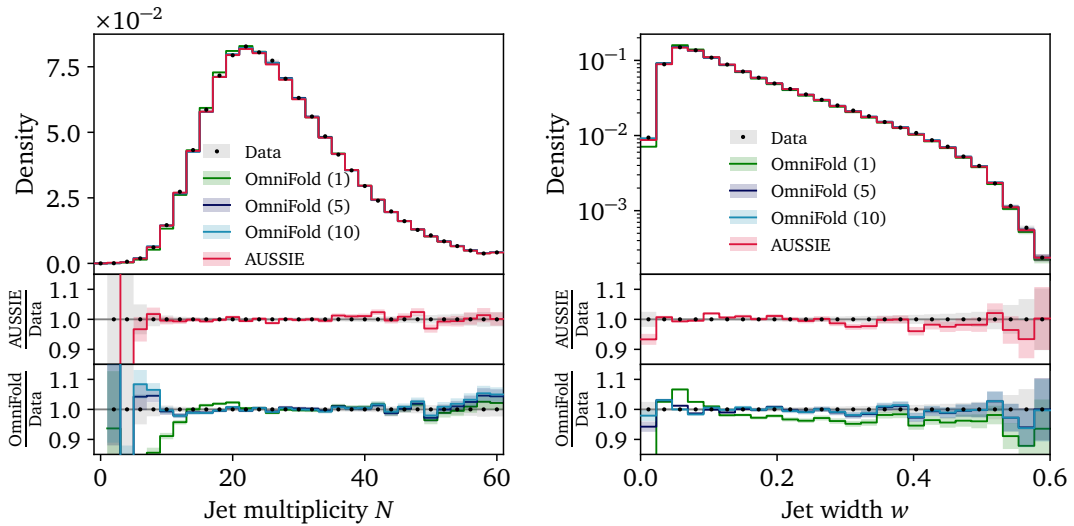


Figure 12: Unfolded part-level jet substructure, comparing AUSSIE and various iterations of OmniFold. Supplements Figure 5.

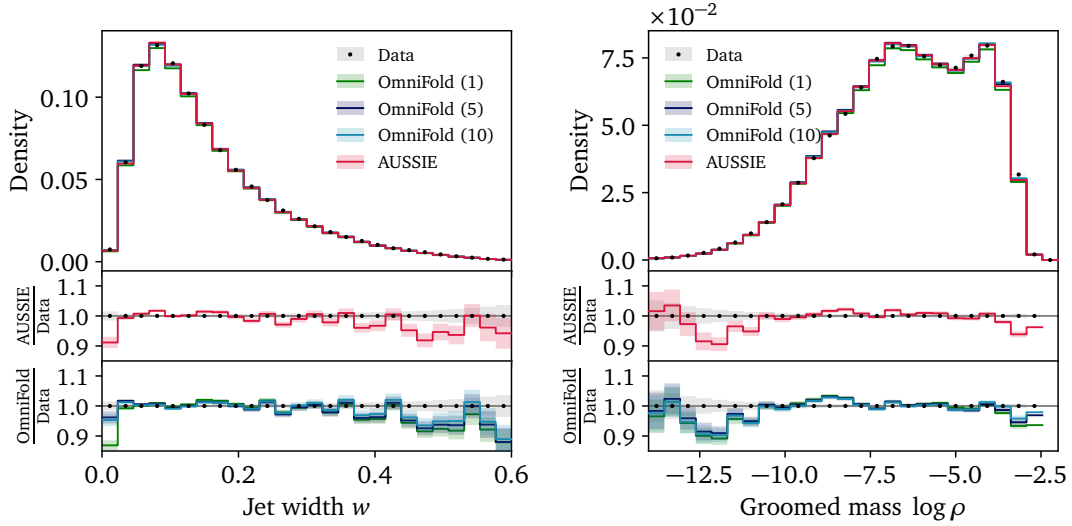


Figure 13: Reco-level jet substructure (using constituents), comparing AUSSIE and various iterations of OmniFold. Supplements Figure 6.

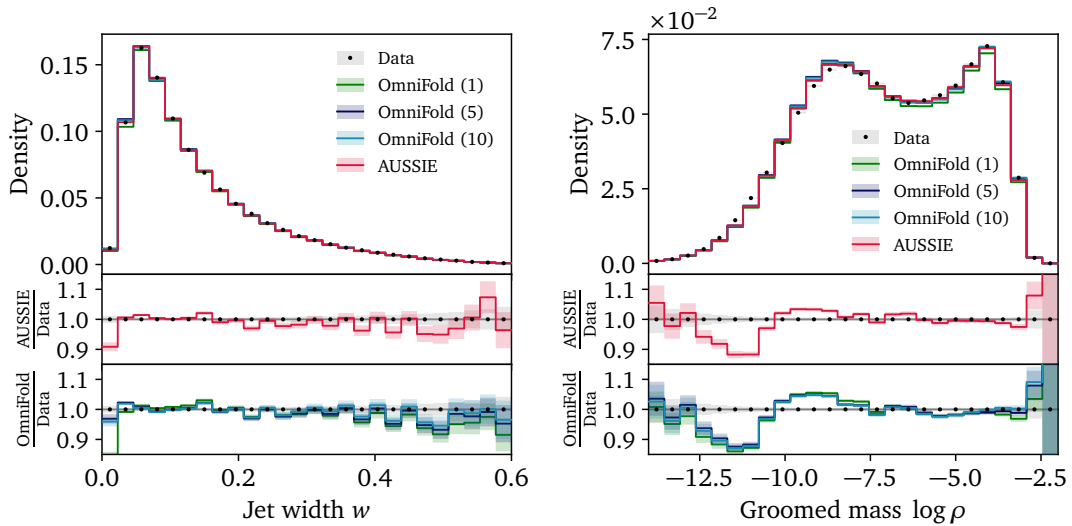


Figure 14: Unfolded part-level jet substructure (using constituents), comparing AUSSIE and various iterations of OmniFold. Supplements Figure 8.

References

- [1] J. M. Campbell *et al.*, *Event generators for high-energy physics experiments*, *SciPost Phys.* **16** (2024) 5, 130, [arXiv:2203.11110 \[hep-ph\]](#).
- [2] G. Cowan, *A survey of unfolding methods for particle physics*, *Conf. Proc. C* **0203181** (2002) 248.
- [3] G. D'Agostini, *Improved iterative Bayesian unfolding*, in *Alliance Workshop on Unfolding and Data Correction*. 10, 2010. [arXiv:1010.0632 \[physics.data-an\]](#).
- [4] S. Schmitt, *TUnfold: an algorithm for correcting migration effects in high energy physics*, *JINST* **7** (2012) T10003, [arXiv:1205.6201 \[physics.data-an\]](#).
- [5] T. Plehn, A. Butter, B. Dillon, T. Heimel, C. Krause, and R. Winterhalder, *Modern Machine Learning for LHC Physicists*, [arXiv:2211.01421 \[hep-ph\]](#).
- [6] N. Huetsch *et al.*, *The landscape of unfolding with machine learning*, *SciPost Phys.* **18** (2025) 2, 070, [arXiv:2404.18807 \[hep-ph\]](#).
- [7] F. Canelli *et al.*, *A practical guide to unbinned unfolding*, *Eur. Phys. J. C* **86** (2026) 2, 106, [arXiv:2507.09582 \[hep-ph\]](#).
- [8] A. Andreassen, P. T. Komiske, E. M. Metodiev, B. Nachman, and J. Thaler, *OmniFold: A Method to Simultaneously Unfold All Observables*, *Phys. Rev. Lett.* **124** (2020) 18, 182001.
- [9] J. Chan and B. Nachman, *Unbinned profiled unfolding*, *Phys. Rev. D* **108** (2023) 1, 016002, [arXiv:2302.05390 \[hep-ph\]](#).
- [10] K. Desai, B. Nachman, and J. Thaler, *Moment extraction using an unfolding protocol without binning*, *Phys. Rev. D* **110** (2024) 11, 116013, [arXiv:2407.11284 \[hep-ph\]](#).
- [11] H. Zhu, K. Desai, M. Kuusela, V. Mikuni, B. Nachman, and L. Wasserman, *Multidimensional Deconvolution with Profiling*, [arXiv:2409.10421 \[hep-ph\]](#).
- [12] A. Falcão and A. Takacs, *High-Dimensional Unfolding in Large Backgrounds*, [arXiv:2507.06291 \[hep-ph\]](#).
- [13] LHCb, R. Aaij *et al.*, *Multidifferential study of identified charged hadron distributions in Z-tagged jets in proton-proton collisions at $\sqrt{s} = 13$ TeV*, *Phys. Rev. D* **108** (2023) L031103, [arXiv:2208.11691 \[hep-ex\]](#).
- [14] H1, V. Andreev *et al.*, *Unbinned deep learning jet substructure measurement in high Q_{2ep} collisions at HERA*, *Phys. Lett. B* **844** (2023) 138101, [arXiv:2303.13620 \[hep-ex\]](#).
- [15] ATLAS, G. Aad *et al.*, *Precision calibration of calorimeter signals in the ATLAS experiment using an uncertainty-aware neural network*, *SciPost Phys.* **19** (2025) 6, 155, [arXiv:2412.04370 \[hep-ex\]](#).
- [16] ATLAS, G. Aad *et al.*, *Measurement of jet track functions in pp collisions at $s = 13$ TeV with the ATLAS detector*, *Phys. Lett. B* **868** (2025) 139680, [arXiv:2502.02062 \[hep-ex\]](#).
- [17] CMS, V. Chekhovsky *et al.*, *Measurement of event shapes in minimum-bias events from proton-proton collisions at $\sqrt{s} = 13$ TeV*, [arXiv:2505.17850 \[hep-ex\]](#).

- [18] Electron-Positron Alliance, A. Badea *et al.*, *Unbinned measurement of thrust in e^+e^- collisions at $\sqrt{s} = 91.2$ GeV with ALEPH archived data*, [arXiv:2510.22038 \[hep-ex\]](#).
- [19] M. Bellagente, A. Butter, G. Kasieczka, T. Plehn, and R. Winterhalder, *How to GAN away Detector Effects*, *SciPost Phys.* **8** (2020) 4, 070, [arXiv:1912.00477 \[hep-ph\]](#).
- [20] M. Bellagente, A. Butter, G. Kasieczka, T. Plehn, A. Rousselot, R. Winterhalder, L. Ardizzone, and U. Köthe, *Invertible Networks or Partons to Detector and Back Again*, *SciPost Phys.* **9** (2020) 074, [arXiv:2006.06685 \[hep-ph\]](#).
- [21] M. Vandegar, M. Kagan, A. Wehenkel, and G. Louppe, *Neural Empirical Bayes: Source Distribution Estimation and its Applications to Simulation-Based Inference*, [arXiv:2011.05836 \[stat.ML\]](#).
- [22] J. N. Howard, S. Mandt, D. Whiteson, and Y. Yang, *Learning to simulate high energy particle collisions from unlabeled data*, *Sci. Rep.* **12** (2022) 7567, [arXiv:2101.08944 \[hep-ph\]](#).
- [23] A. Shmakov, K. Greif, M. Fenton, A. Ghosh, P. Baldi, and D. Whiteson, *End-To-End Latent Variational Diffusion Models for Inverse Problems in High Energy Physics*, [arXiv:2305.10399 \[hep-ex\]](#).
- [24] S. Diefenbacher, G.-H. Liu, V. Mikuni, B. Nachman, and W. Nie, *Improving generative model-based unfolding with Schrödinger bridges*, *Phys. Rev. D* **109** (2024) 7, 076011, [arXiv:2308.12351 \[hep-ph\]](#).
- [25] A. Shmakov, K. Greif, M. J. Fenton, A. Ghosh, P. Baldi, and D. Whiteson, *Full Event Particle-Level Unfolding with Variable-Length Latent Variational Diffusion*, [arXiv:2404.14332 \[hep-ex\]](#).
- [26] C. Pazos, S. Aeron, P.-H. Beauchemin, V. Croft, Z. Huan, M. Klassen, and T. Wongjirad, *Towards Universal Unfolding of Detector Effects in High-Energy Physics using Denoising Diffusion Probabilistic Models*, [arXiv:2406.01507 \[physics.data-an\]](#).
- [27] A. Butter, S. Diefenbacher, N. Huetsch, V. Mikuni, B. Nachman, S. Palacios Schweitzer, and T. Plehn, *Generative unfolding with distribution mapping*, *SciPost Phys.* **18** (2025) 6, 200, [arXiv:2411.02495 \[hep-ph\]](#).
- [28] L. Favaro, R. Kogler, A. Paasch, S. Palacios Schweitzer, T. Plehn, and D. Schwarz, *How to unfold top decays*, *SciPost Phys. Core* **8** (2025) 053, [arXiv:2501.12363 \[hep-ph\]](#).
- [29] A. Butter, T. Heimel, N. Huetsch, M. Kagan, and T. Plehn, *Simulation-Prior Independent Neural Unfolding Procedure*, [arXiv:2507.15084 \[hep-ph\]](#).
- [30] A. Petitjean, A. Butter, K. Greif, S. Palacios Schweitzer, T. Plehn, J. Spinner, and D. Whiteson, *Generative Unfolding of Jets and Their Substructure*, [arXiv:2510.19906 \[hep-ph\]](#).
- [31] M. Backes, A. Butter, M. Dunford, and B. Malaescu, *An unfolding method based on conditional invertible neural networks (cINN) using iterative training*, *SciPost Phys. Core* **7** (2024) 1, 007, [arXiv:2212.08674 \[hep-ph\]](#).
- [32] K. Datta, D. Kar, and D. Roy, *Unfolding with Generative Adversarial Networks*, [arXiv:1806.00433 \[physics.data-an\]](#).

- [33] ATLAS, G. Aad *et al.*, *Simultaneous Unbinned Differential Cross-Section Measurement of Twenty-Four Z+jets Kinematic Observables with the ATLAS Detector*, *Phys. Rev. Lett.* **133** (2024) 26, 261803, [arXiv:2405.20041 \[hep-ex\]](#).
- [34] A. Butter, N. Huetsch, V. Mikuni, B. Nachman, and S. Palacios Schweitzer, *Analysis-ready Generative Unfolding*, [arXiv:2509.02708 \[hep-ph\]](#).
- [35] H. Zhu, K. Desai, M. Kuusela, V. Mikuni, B. Nachman, and L. Wasserman, *Machine Learning-based Unfolding for Cross Section Measurements in the Presence of Nuisance Parameters*, [arXiv:2512.07074 \[stat.AP\]](#).
- [36] D. Valsecchi, M. Donegà, and R. Wallny, *Profiling systematic uncertainties in Simulation-Based Inference with Factorizable Normalizing Flows*, [arXiv:2602.13184 \[hep-ph\]](#).
- [37] A. Jacot, F. Gabriel, and C. Hongler, *Neural tangent kernel: Convergence and generalization in neural networks*, in *Advances in Neural Information Processing Systems*. 2018. [arXiv:1806.07572 \[cs.LG\]](#).
- [38] A. Chiefa, L. Del Debbio, and R. Kenway, *Quantitative Understanding of PDF Fits and their Uncertainties*, [arXiv:2512.24116 \[hep-ph\]](#).
- [39] DELPHES 3, J. de Favereau, C. Delaere, P. Demin, A. Giammanco, V. Lemaître, A. Mertens, and M. Selvaggi, *DELPHES 3, A modular framework for fast simulation of a generic collider experiment*, *JHEP* **02** (2014) 057, [arXiv:1307.6346 \[hep-ex\]](#).
- [40] J. Brehmer, V. Bresó, P. de Haan, T. Plehn, H. Qu, J. Spinner, and J. Thaler, *A Lorentz-equivariant transformer for all of the LHC*, *SciPost Phys.* **19** (2025) 4, 108, [arXiv:2411.00446 \[hep-ph\]](#).
- [41] A. Petitjean, T. Plehn, J. Spinner, and U. Köthe, *Economical Jet Taggers – Equivariant, Slim, and Quantized*, [arXiv:2512.17011 \[hep-ph\]](#).
- [42] W. Bhimji, C. Harris, V. Mikuni, and B. Nachman, *OmniLearned: A Foundation Model Framework for All Tasks Involving Jet Physics*, [arXiv:2510.24066 \[hep-ph\]](#).
- [43] V. Mikuni and B. Nachman, *Method to simultaneously facilitate all jet physics tasks*, *Phys. Rev. D* **111** (2025) 5, 054015, [arXiv:2502.14652 \[hep-ph\]](#).
- [44] V. Mikuni and B. Nachman, *Solving key challenges in collider physics with foundation models*, *Phys. Rev. D* **111** (2025) 5, L051504, [arXiv:2404.16091 \[hep-ph\]](#).
- [45] A. Butter, T. Heimel, T. Martini, S. Peitzsch, and T. Plehn, *Two invertible networks for the matrix element method*, *SciPost Phys.* **15** (2023) 3, 094, [arXiv:2210.00019 \[hep-ph\]](#).
- [46] T. Heimel, N. Huetsch, R. Winterhalder, T. Plehn, and A. Butter, *Precision-machine learning for the matrix element method*, *SciPost Phys.* **17** (2024) 5, 129, [arXiv:2310.07752 \[hep-ph\]](#).
- [47] A. Butter, S. Diefenbacher, G. Kasieczka, B. Nachman, T. Plehn, D. Shih, and R. Winterhalder, *Ephemeral Learning - Augmenting Triggers with Online-Trained Normalizing Flows*, *SciPost Phys.* **13** (2022) 4, 087, [arXiv:2202.09375 \[hep-ph\]](#).